RSC
Mechanochemistry

PAPER

View Article Online
View Journal

Cite this: DOI: 10.1039/d5mr00092k

Mechanistic investigation of the mechanochemical reduction of $LiCoO_2$ with Al in the context of lithium-ion battery recycling

Raphael Sieweck,[a] Arseniy Bokov,[ab] Oleksandr Dolotko,[ab] Thomas Bergfeldt,[a] Udo Geckle,[a] Michael Knapp[a] and Helmut Ehrenberg[ab]

Received 7th July 2025
Accepted 3rd December 2025

DOI: 10.1039/d5mr00092k

rsc.li/RSCMechanochem

Lithium-ion batteries are the most common energy storage system for consumer electronics and electric vehicles, and are now emerging into the market for stationary applications. However, their production depends on critical raw materials, such as lithium, nickel, and cobalt. When reaching the end of their life, spent batteries are regarded as toxic waste, underscoring the need for efficient and inexpensive recycling technologies to enable a circular economy. Current recycling technologies exhibit issues, such as wastewater generation and high consumption of energy and chemicals. While the focus has been on the recovery of valuable transition metals, lithium is often not recovered. In this study, we present a deeper investigation of the solvent-free mechanochemical reduction of $LiCoO_2$ with Al. The combined analysis using XRD, SEM and EDX, together with the observation of a characteristic temperature and pressure profile, proved the reaction to proceed *via* a mechanically induced self-propagating reaction pathway. A spike in the pressure, detected by an internal sensor in the milling jar, was used to determine the length of the activation phase, which enables a kinematic analysis and the systematic study of milling parameters. Furthermore, the presence of graphite was found to increase the activation time and with a 20% weight fraction, the self-propagating behavior can be suppressed. This research provides important information regarding the application of this process on a real black mass or on a larger scale.

Open Access Article. Published on 15 December 2025. Downloaded on 1/7/2026 11:21:34 AM.
This article is licensed under a Creative Commons Attribution 3.0 Unported Licence.

Introduction

A substantial increase in lithium-ion battery (LIB) waste is anticipated in the coming years, mainly driven by the growing number of electric vehicles (EVs) reaching the end of their life.[1] This situation necessitates the development of more efficient recycling methods. The conventional industrial processes are designed around the recovery of valuable transition metals, while the extraction of lithium (Li) remains challenging.[2] Therefore, the development of novel recycling concepts is essential to avoid lithium losses and contribute to the circular economy.

Lithium is indispensable for the production of LIBs, and its demand is experiencing a pronounced increase. Nowadays, lithium is primarily extracted from brines in South America or through mining activities in Australia.[3] Although recent discoveries in Europe have identified additional lithium reserves, the European Union (EU) has classified it as a critical raw material.[4] The recovery of Li from batteries can help to address the growing demand, reduce reliance on non-European sources, and ensure compliance with the EU's regulations concerning battery production and utilization.[5–8]

In LIBs, Li is present in the cathode active material (CAM), which is coated on an aluminum current collector, and in the conductive salt, dissolved in the electrolyte. After collecting the end-of-life (EoL) EV batteries, several pretreatment steps are usually performed, including sorting, discharging, and dismantling.[9] Subsequent shredding facilitates the separation of components based on their physical properties, such as density, magnetism, and size. One of the fractions obtained is a fine powder known as black mass, which contains the active materials from both the anode and cathode, along with impurities from other components, and serves as starting material for further chemical recycling.[10]

Pyrometallurgical processes operate at temperatures above 1000 °C to induce carbothermal reduction, but they suffer from a high energy consumption and the emission of toxic gas. The transition metals are recovered as alloys, while lithium is usually lost to the slag. In hydrometallurgical processes, the Li-containing CAMs are dissolved in acids, and the transition metals are subsequently recovered by precipitation or solvent extraction.[11] Nonetheless, Li can still be partially lost by co-precipitation or co-extraction and may become contaminated with process chemicals. New approaches are also being explored with a focus on electrochemical methods or thermal pre-treatments.[12]

---

[a] Karlsruhe Institute of Technology (KIT), Institute for Applied Materials (IAM), Hermann-von-Helmholtz-Platz 1, D-76344 Eggenstein-Leopoldshafen, Karlsruhe, Germany

[b] Helmholtz-Institute Ulm for Electrochemical Energy Storage (HIU), P. O. Box 3640, D-76021 Karlsruhe, Germany

© 2025 The Author(s). Published by the Royal Society of Chemistry

Open Access Article. Published on 15 December 2025. Downloaded on 1/7/2026 11:21:34 AM. This article is licensed under a Creative Commons Attribution 3.0 Unported Licence.

Recently, mechanochemical routes have been developed to process the CAMs together with Cu or Al as reactants,[13–15] followed by the selective extraction of Li *via* acid-free aqueous leaching and the recovery of transition metals through low-concentration acid leaching.[16] In mechanochemical reactions, the kinetic energy is transferred to the starting materials, thereby enabling the solid-state reactions at ambient temperatures.[17] As it has been reported by Dolotko *et al.*, common CAMs including $LiCoO_2$ (LCO), $LiMn_2O_3$ (LMO), $LiNi_xMn_yCo_zO_2$ (NMC), and $LiFePO_4$ (LFP) can be reduced with Al in a high-energy shaker mill.[13,18] The strong reducing agent Al, which is already present in a LIB as the current collector, undergoes an exothermic thermite-like reaction with transition metal oxides. Although this process is hindered by high activation energy,[19] the mechanical forces inherent in a high-energy ball mill can overcome the activation barrier and induce the reaction.[20–22]

In the literature,[23,24] similar highly exothermic mechanochemical experiments are described as mechanically induced self-propagating reactions (MSR), which is divided into three stages. First, collisions, friction, and shear activate the powder during milling. This initial phase leads to a reduction in primary particle size, thorough mixing, and distortion of the crystal structure, but little or no chemical transformation occurs. The activated powder then begins to agglomerate, and eventually, the kinetic energy of a collision triggers a reaction, marking the start of the second stage. The released heat ignites the surrounding powder and initiates a combustion front that propagates through the entire reaction volume. Subsequently, further milling is employed to refine the products.[21,24] The self-propagating behavior of the highly exothermic reaction results in an extremely rapid increase in temperature and, consequently, an increase in internal pressure.[25,26] Both parameters can be measured *in situ* to determine the exact onset of the reaction.

After Dolotko *et al.*[18] reported the mechanochemical reduction of common CAMs in a shaker mill, Vauloup[27] systematically investigated the influence of milling parameters on the reduction of LCO with Al in a planetary ball mill. Specifically, a temperature increase in the milling jar and the formation of large metallic pieces were observed after a certain period.[27] However, the actual reaction mechanism was not completely elaborated and no quantitative analysis of introduced milling energy was provided yet. To bridge this knowledge gap and improve understanding of the high-energy milling processing, the present work investigates mechanochemical reactions in the $LiCoO_2$–Al model system. The study aims to clarify the influence of key variables at a quantitative level and to investigate the underlying reaction mechanism. Furthermore, it explores the effect of graphite on the reaction profile, which is essential for practical applications such as scaling up the process or its adaption to the industrial black mass.

Materials and methods

Materials

The starting materials for this study were obtained from the following suppliers. The $LiCoO_2$ powder (97%) was purchased from Thermo Fisher Scientific, metallic Aluminum powder (−325 mesh, 99.5%) from Alfa Aesar, and the battery grade graphite from Imerys Graphite & Carbon. All materials were used as received.

The LCO cathode material was selected for this study, because layered oxides are commonly used cathode materials in LIBs and the small number of elements facilitate the analysis. Based on standard formation enthalpies, oxidation states and the identical crystal structure, layered oxide materials with the formula $LiNi_xCo_yMn_zO_2$, with $x + y + z = 1$, are expected to react similarly. Metallic Al was used as the reducing agent because it is cheap and already present in LIBs as the current collector, which might reduce the operating costs. Although, the current collector is a foil, a powder was used in the present work to suppress the influence of different particle sizes. Al is a strong reducing agent, which provides 3 electrons but is covered with an inert aluminum oxide layer allowing safe handling in air and finally the utilization of Al allows the comparison to previous literature.[13,15,18,27]

Mechanochemical experiments

All experiments were performed in a Pulverisette 7 premium line (Fritsch GmbH) planetary mill using an 80 mL stainless-steel milling jar (440C/X105CrMo17 grade) equipped with an

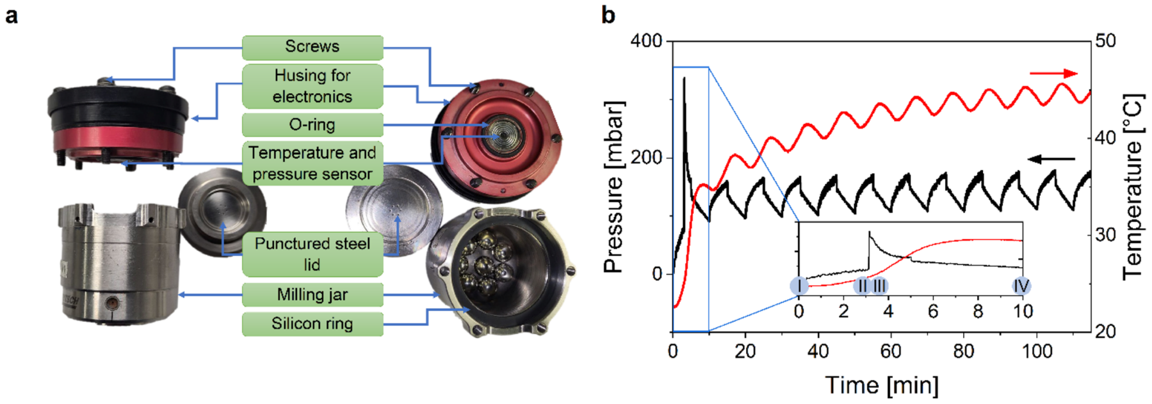

Fig. 1 (a) Experimental setup and (b) recorded pressure and temperature curves during the mechanochemical reaction of LCO and Al at 650 rpm with 60 balls (6.35 mm), 2.0 g of powder, LCO/Al = 1.0 and a SBR of 0.033 using repeating cycles of 5 min milling and 5 min resting.

© 2025 The Author(s). Published by the Royal Society of Chemistry

Open Access Article. Published on 15 December 2025. Downloaded on 1/7/2026 11:21:34 AM.
This article is licensed under a Creative Commons Attribution 3.0 Unported Licence.

EasyGTM® lid to monitor the internal temperature and pressure. As shown in Fig. 1a, the milling jar is closed with a punctured stainless-steel lid and sealed with a silicon ring. A plastic housing containing the electronics and the sensor for temperature and pressure is placed on top of the steel lid and the device is sealed airtight by six screws. The steel lid protects the sensor from collisions with balls and particles but the small holes enable an exchange with the atmosphere in the milling jar and allow the measurement of the internal temperature and pressure.

Before all experiments, an 80 mL stainless steel vial was loaded with about 65 g of steel balls and the respective amount of powder inside the argon filled glovebox. Three different ball diameters were used in this study, namely 3 mm, 6.35 mm and 12.7 mm corresponding to a ball mass of 0.109 g, 1.011 g and 8.202 g respectively. Based on the exact total ball mass, the required amount of powder was calculated according to the respective sample-to-ball ratio (SBR) using 78.39 wt% LCO and 21.61 wt% Al powder, which represents a 1 : 1 molar ratio. Unless stated otherwise, an SBR of 0.033 was used for most experiments.

After loading the milling vial, the powder was properly mixed with a spatula to prevent strong local concentration differences during the first milling seconds, and then the vial was sealed gas-tight. The milling was performed in alternating cycles of 5 min at the experiment-specific speed, followed by 5 min of rotation at 150 rpm to allow the machine to cool down. When a rotation speed of 200 rpm was used, the duration of cooling was reduced to 1 min. The reported milling times refer to the total time excluding the cooling cycles. A detailed list of the reaction parameters is presented in the SI.

Characterization

The phase composition of the milled materials was carried out using X-ray powder diffraction (XRD) on a STOE Stadi P powder diffractometer with Mo-K$_{\alpha 1}$ radiation ($\lambda = 0.70932$ Å) in transmission geometry. Before the analysis, the powdered samples were deposited onto adhesive Kapton foils. The XRD measurements were performed at room temperature with a step of 0.015° between 5 and 35 degrees of 2 Theta.

The morphology of the processed materials was studied by scanning electron microscopy (SEM) in combination with energy-dispersive X-ray spectroscopy (EDX) on a Zeiss Merlin setup with Gatan detector. Images with EDX overlay were plotted using HyperSpy package for python 3.[28] Optical light microscopy was performed on a LEICA M205 C, equipped with a camera.

The elemental analysis of the obtained materials was performed using Inductively Coupled Plasma Optical Emission Spectroscopy (ICP-OES) on an iCAP 7600 DUO (Thermo Fisher Scientific). Samples were dissolved with acid in a graphite oven.

Results and discussion

Evolution of the reaction

The mechanochemical reduction of pristine $LiCoO_2$ with metallic Al was carried out in a planetary ball mill equipped with stainless steel vials and an EasyGTM® lid to monitor the internal pressure and temperature (Fig. 1a). With this setup, the pressure and temperature can be measured *in situ*, with data points collected every 1–2 seconds, providing a good time resolution. The stoichiometry of the reactions during experiments was planned according to the following equation:

$$LiCoO_2 + Al \rightarrow Co + LiAlO_2$$

The recorded profiles in Fig. 1b show a zigzag course, produced by the alternating milling and resting cycles of five min each. Within the first milling cycle, a spike in the pressure curve is noticeable after 3.2 min. The temperature starts to rise from the beginning, even before the spike in pressure. To exclude the contribution of the milling itself to the temperature, the temperature profile of a blank experiment was subtracted from the reaction profile, revealing an increase of about 4.5 °C with an onset at 3.2 min (Fig. S1). The pressure spike was used as a reaction marker to analyze the experiment at specific time points, and samples were collected according to Table 1 (their subsequent analysis is discussed in the following).

To gain deeper insight into the reduction process, samples recovered after different milling times were analyzed by SEM and EDX (Fig. 2). Before milling, the gray powder of mixed starting materials in Sample I consists of well distinguishable particles between 3 and 15 μm with a small contact area. The Al particles can be clearly distinguished from a mixed Co–O containing phase (Fig. 2a–e). Sample II, obtained just before the spike in pressure, is a fine black powder. Within this first period of 2.7 min, the crystallite sizes are reduced and agglomerates are formed, which contain all three elements (Fig. 2f–j).

For a better analysis of the elemental distribution in the agglomerates, the powder was cast in resin, cut and polished to obtain a smooth surface of the cross section. It shows a coarse matrix with capsules of a few microns in diameter, which break off during the cutting and reveal a nanoscale needle-like structure inside with high oxygen content (Fig. 3a). In the EDX maps, the signals from oxygen and cobalt still overlap, while Al is separated from the rest of elements (Fig. 3b). However, the Co–O and the Al phases are mixed on the nanoscale, forming a lamellar structure.

Immediately after the increase in pressure the mill was stopped to collect Sample III. An inhomogeneous mixture of

Table 1 Samples taken from the mechanochemical reaction of LCO and Al at 650 rpm with 60 balls (6.35 mm), 2.0 g of powder, LCO/Al = 1.0 and a SBR of 0.033 using repeating cycles of 5 minutes milling and 5 min resting

Sample	Total time [min]	Description
I	0	Before milling
II	2.7	Shortly before pressure spike
III	3.2	Directly after pressure spike
IV	15	After 10 min of milling
V	115	After 60 min of milling

Open Access Article. Published on 15 December 2025. Downloaded on 1/7/2026 11:21:34 AM.
This article is licensed under a Creative Commons Attribution 3.0 Unported Licence.

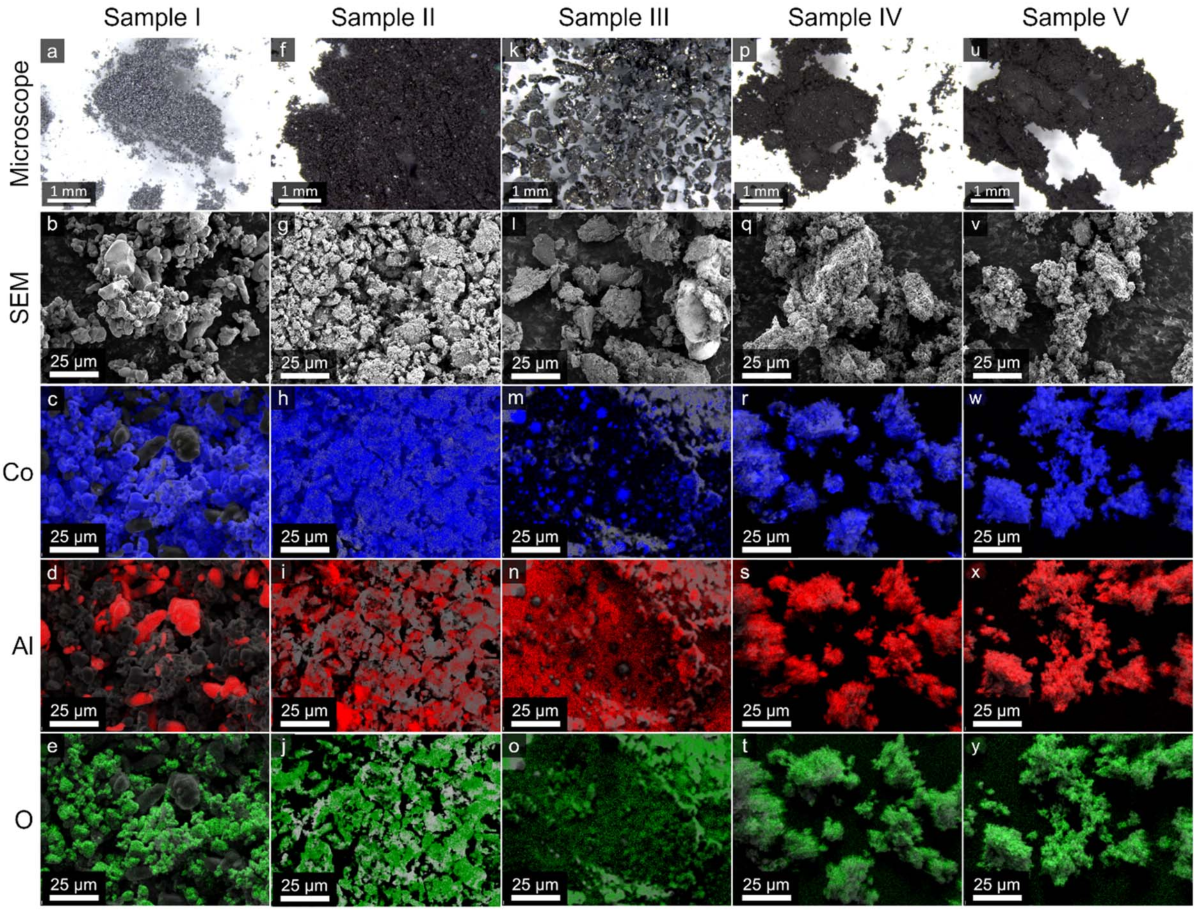

Fig. 2 Microscopy images and respective EDX images for Co (blue), Al (red) and O (green) of the Samples I–V (a–e, f–j, k–o, p–t and u–y, respectively) collected during the mechanochemical reaction between LCO and Al at 650 rpm with 60 balls (6.35 mm), 2.0 g of powder, LCO/Al = 1.0 and a SBR of 0.033 using repeating cycles of 5 min milling and 5 min resting.

coarse gray powder and metallic pieces up to the centimeter scale was obtained. In the SEM (Fig. 2l) particles with smooth surfaces and sharp edges can be distinguished from smooth spheres and porous agglomerates. The EDX micrographs show a partial separation of spherical cobalt pieces from the aluminum phase (Fig. 2m–o). The mixture was sieved and the fraction smaller than 500 µm was cast in resin and cut to obtain a smooth cross section, which allows a better analysis of the elemental distribution (Fig. 3c and d).

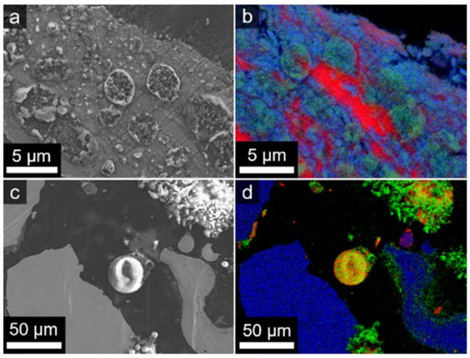

Fig. 3 SEM and EDX images of cross sections of Sample II (a and b) and Sample III (c and d). Co, Al and O are presented in blue, red and green color respectively.

Much larger particles are present in Sample III (Fig. 3c, d and S2) than in Sample II (Fig. 3a and b) and they can be roughly divided into a cobalt phase, an aluminum oxide phase and agglomerates of intensively mixed starting material, similar to the agglomerates in Sample II. In Fig. 3d, the Co-phase shows only a weak signal from aluminum and oxygen. Its surface appears smooth, with clearly visible grain boundaries and small spherical holes, suggesting the former presence of an inclusion. The Al–O phases have almost no contribution from cobalt. Some particles show a rough surface with crystalline needles, which might have formed by the reaction with humid air and others are spherical which could indicate partial melting during the reaction. These small spherical particles are most likely responsible for the spherical holes in the cobalt phase.

After 10 min of milling, the large pieces were crushed and Sample IV became a homogeneous fine black powder again. The signals from Co, Al and O are distributed in all agglomerates with some local enrichment in cobalt (Fig. 2p–t). With further milling, Sample V resembles Sample IV but with slightly smaller

Open Access Article. Published on 15 December 2025. Downloaded on 1/7/2026 11:21:34 AM.
This article is licensed under a Creative Commons Attribution 3.0 Unported Licence.

secondary particles and fewer localized high-intensity signals from any element (Fig. 2u–y). However, prolonged milling times result in an increased presence of iron and chromium in the EDX spectra, attributed to abrasion of the milling balls (Fig. S3).

The evolution of phase composition in the five samples was analyzed by XRD. Before milling, the mixture in Sample I consists of two distinct crystallographic phases, namely $LiCoO_2$ and Al (Fig. 4, 0 min). The XRD pattern of Sample II does not show any new reflections, indicating that little or no chemical reaction has occurred, but the peaks become much broader representing size reduction and an increase in stress (Fig. 4a, 2.7 min). However, after only 30 s of further milling and directly after the spike in pressure, the XRD patterns of Sample III indicate a considerable evolution of peaks (Fig. 4a, 3.2 min). Tetragonal γ-$LiAlO_2$ in the space group $P4_12_12$ (No. 92) has formed as a new phase with sharp reflections and elemental cobalt is present in a cubic closed-packed structure corresponding to the space group $Fm\bar{3}m$ (No. 225) and hexagonal structure described by the space group $P63/mmc$ (No. 194). The cubic phase of cobalt is its high temperature modification and is usually thermodynamically stable above 450 °C. However, the observation of the cubic phase at room temperature could be explained either by the presence of nanocrystalline domains[29] or a by a stabilization due to impurity atoms[30] or mechanical strain.[31,32] The starting materials LCO and Al are still present in small amounts and some new reflections can be assigned best to a cubic Li-deficient $Li_{(0-0.2)}Co_{(0.8-1)}O$ phase[33] in the space group $Fm\bar{3}m$ (No. 225).

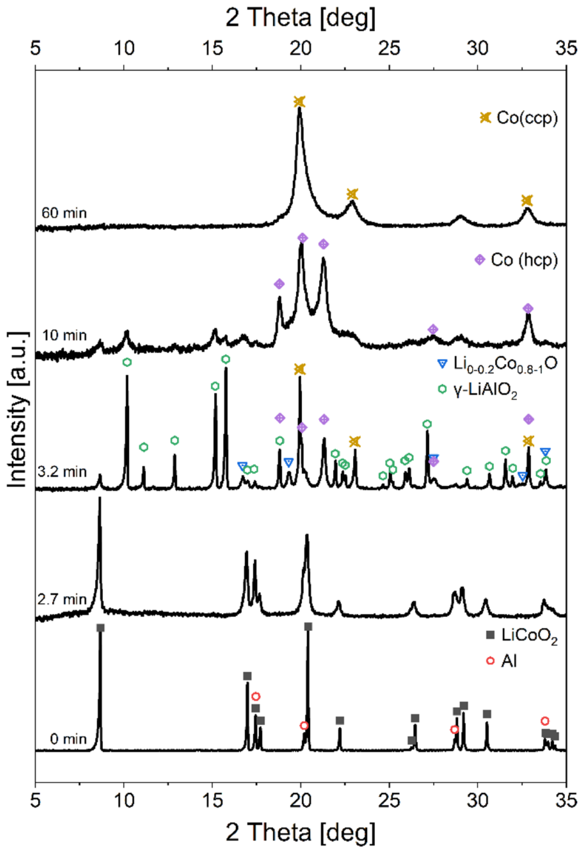

Fig. 4 Evolution of XRD patterns for the Samples I–V, collectd during the mechanochemical reaction between LCO and Al at 650 rpm with 60 balls (6.35 mm), 2.0 g of powder, LCO/Al = 1.0 and a SBR of 0.033 using repeating cycles of 5 min milling and 5 min resting.

In Sample IV, the reflections of both Co phases become dominant in the XRD pattern (Fig. 4a, 10 min), while the $LiAlO_2$ reflections are difficult to identify due to significant broadening resulting from amorphization. With further milling, the broadening of the peaks is more pronounced and only four reflections are visible in Sample V (Fig. 4, 60 min). The presence of broad, undefined, or absent reflections suggest that the phases are highly strained, and have small domain sizes. Three of the visible reflections can be assigned to a nanocomposite of cubic Co metal. Due to the undefined peaks, no phase was found to fit well for the reflection at 29.3° of 2 Theta. Vauloup[27] proposed a cubic CoFe alloy in the space group $Im\bar{3}m$ (No. 229) which would show reflections at 20.3° and 28.9° of 2 Theta. This seems reasonable, as the first and most intense reflection shows an asymmetry on the high angle side, while one of the peaks at 29.3° of 2 Theta is slightly shifted, potentially caused by a different stoichiometric composition. Further, iron and chromium which are introduced by abrasion, were detected in EDX spectra (Fig. S2) and in the ICP-OES analysis of the reaction products, milled for 60 min (Table S7) and verify the possible presence of the CoFe alloy in the mixture.

The larger metallic pieces in Sample III can be separated using a 500-µm sieve, and the attached particles can be removed through sonication in deionized water. The XRD analysis of such a metallic piece reveals the presence of cobalt in the hcp structure (No. 194), alongside with a minor amount of its cubic phase (No. 225) (Fig. 5). No other phases are visible and based on the ICP-OES analysis (Table S7), the metallic piece is composed of 97% (±1.9) Co and only of 0.24% Al. The residual mass was not identified by ICP-OES and is assumed to correspond to oxygen or iron.

The results above clearly indicate that all transformations occur according to the MSR mechanism.[24,34,35] Before the

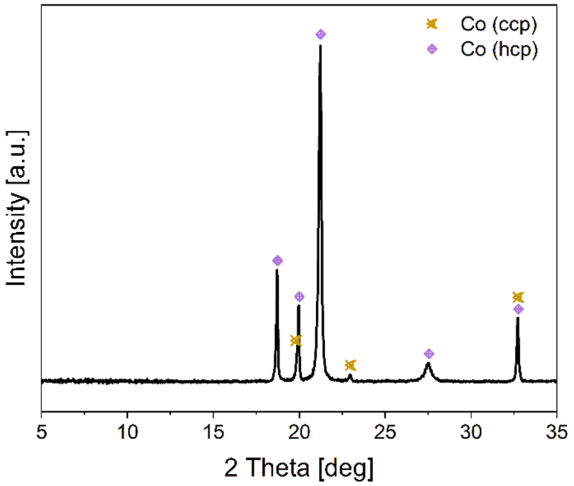

Fig. 5 XRD pattern of an isolated metallic piece, collected after 3.2 min of milling LCO and Al at 650 rpm using 60 balls (6.35 mm), 2.0 g of powder, LCO/Al = 1.0 and a SBR of 0.033.

Open Access Article. Published on 15 December 2025. Downloaded on 1/7/2026 11:21:34 AM. This article is licensed under a Creative Commons Attribution 3.0 Unported Licence.

increase in pressure, the starting materials in Sample II were thoroughly mixed and the crystals were fractured by the collisions. The XRD analysis indicates that the crystallites decreased in size and experienced strain while merging into large agglomerates. At this stage, an activated mixture is formed from the starting materials, but no reaction is detected yet. This activation reduces the energy required to initiate a reaction until it reaches a threshold and a collision with powder trapped between a ball and the wall provides sufficient energy to initiate the reaction (Sample III). The heat released by the exothermic reaction provides the thermal energy needed to trigger further reactions in the surrounding powder, leading to self-heating. As a result, a reaction front spreads through the entire volume, releasing more heat in a short time. During this fast high-temperature reaction, well crystalline phases of $LiAlO_2$ and metallic cobalt are formed, but when the milling is continued, the collisions lead to particle size reduction and distortion of the crystallites. In consequence, hexagonal cobalt transforms into the cubic phase and the product mixture becomes appears amorphous. The amorphization is faster for the brittle $LiAlO_2$ than for the ductile cobalt.

In thermite-like reactions, the internal temperature usually exceeds the products melting points, which are 1495 °C and 1625 °C for Co and $LiAlO_2$, respectively,[36,37] and is limited by the products lowest boiling point. However, the high thermal conductivity of the stainless-steel milling media allows a fast heat dissipation, preventing the internal temperature from attaining such elevated values. The reaction mixture could be locally molten at the particle scale, and the different phases separate to produce an almost pure metallic cobalt fraction, alongside the $LiAlO_2$ fraction. The fast reaction kinetics cause a rapid temperature rise, leading to gas expansion, which result in a sudden increase in internal pressure in the sealed milling jar. Heat dissipation then cools the reactants quickly, allowing the system to return to a moderate temperature and pressure. In the EasyGTM design, the temperature and pressure sensors are well protected in the lid. This arrangement allows the pressure increase can be tracked immediately, while the temperature curve is damped and measured with a delay. Although the sensors transmit data every 1–2 seconds, the time for the MSR event can be detected accurately, though maximal pressure may occur between measuring points and can exceed the detected value. The heat from the reaction spreads into the milling media, and only the average temperature increase of the milling vial is observed. Under such conditions, the reaction front might not reach all the starting material, requiring further milling to complete the reaction. Continued milling breaks down the metallic particles and coarse agglomerates, forming a finely mixed powder.

The rapid reaction kinetics associated with the MSR process might pose significant challenges when attempting to scale up for industrial application, as the abrupt temperature changes impose limitations on the materials that can be used. Ceramics, such as ZrO_2 can fracture due to these rapid temperature changes,[38] potentially leading to contamination and increased operating costs, as the grinding media must be replaced frequently. More durable materials like steel are less prone to failure, but during the high-temperature stage, collisions can lead to deformation of the grinding balls. This results in increased abrasion, especially when large, cobalt particles are present. Indeed, after many experiments, a small number of balls showed indentations. In addition to the high temperature, the milling reactor must also withstand abrupt increases in pressure to ensure safe operation.

Despite the challenges posed by the MSR mechanism, the resulting pressure spike can be used to investigate how milling parameters affect the activation time. This can be achieved through a kinematic analysis, which might prove beneficial for optimizing the reaction and allows the comparison to other reactions and milling types.

Kinematic analysis

As follows from the XRD analysis, the majority of the starting mixture reacts after the activation phase within less than a second, which is consistent with Vauloups observations.[27] The length of the activation phase can be accurately determined with the onset of the spike in pressure. This onset is called ignition time (t_{ig}) and marks the initiation of the fast, self-propagating reaction. During the activation phase, the starting powders are mixed and crushed by repeated collisions. The collision frequency and the impact energy, which depend on the ball's velocity, mass and the number of balls, affect the t_{ig} parameter directly.[39]

With the kinematic equations, derived by Burgio[40] and adapted by Kessler for the Pulverisette 7 (Fritsch),[41] the impact energies and frequencies can be calculated and used to evaluate the effect of milling parameters. However, it should be noted that such model neglects the influence of friction, which could have a notable contribution to the transferred energy in planetary ball mills.[40,42,43] All the equations used and respective parameters are presented in the SI.

At first, the influence of the rotation speed (ν_R) on the ignition time (t_{ig}) was investigated within the range of 200 to 950 rpm (Fig. 6a). Triplicates were performed for each rotation speed, but the respective ignition times shown in Fig. 6a reveal almost no deviation between identical experiments, appearing as single entries with the exception of those performed at 200 rpm. Assuming a purely inelastic collision model, the kinetic energy transferred from one ball to the powder (ΔE_b^*) by a single collision can be calculated according to eqn (1), taking the mass (m_b) and diameter (d_b) of a milling ball, the radius of the central plate (R_P) and of the milling jar (R_J) and the ν_R into account. Additionally, it should be corrected with the yield coefficient (φ_b) to include the ball-to-ball interactions. According to eqn (2), the number of total collisions (N_{tot}) can be determined by considering the collision frequency (f_b), the number of balls (N_b) and t_{ig}. The eqn (1) and (2) imply, that ΔE_b^* and N_{tot} should depend on the rotation speed to the power of 2 and the power of 1 respectively.

Furthermore, the milling energy accumulated up to the t_{ig} should be invariable, irrespective of the rotational speed,[44] while in contrast t_{ig}, should depend on the power of −3 on ν_R. However, when the measured t_{ig} values were fitted with

© 2025 The Author(s). Published by the Royal Society of Chemistry

Open Access Article. Published on 15 December 2025. Downloaded on 1/7/2026 11:21:34 AM. This article is licensed under a Creative Commons Attribution 3.0 Unported Licence.

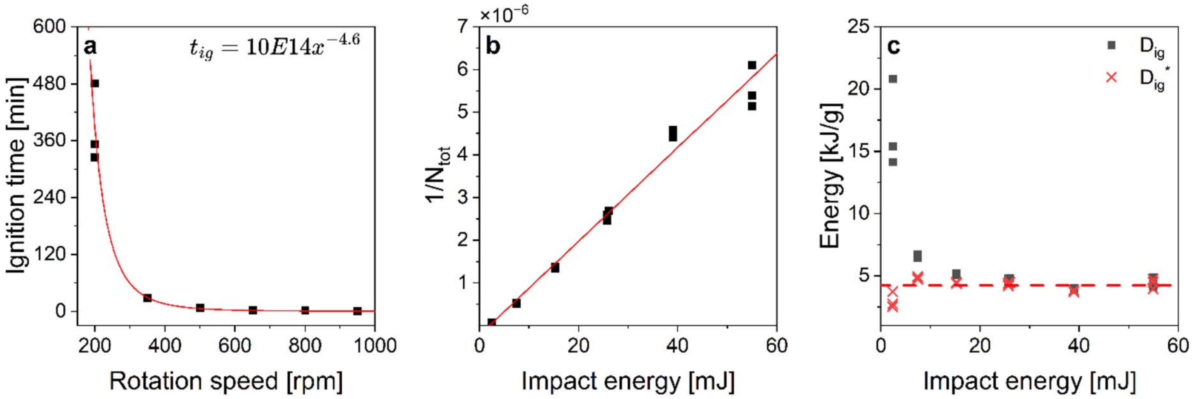

Fig. 6 Influence of the rotation speed on the mechanochemical reaction of LCO with Al using 65 balls (6.35 mm), 2.1 g of powder, LCO/Al = 1.0 and a SBR of 0.033 with repeating cycles of 5 minutes milling and 5 min resting. (a) ignition time (t_{ig}) *vs.* rotation speed (ν_R), (b) reciprocal number of collisions (N_{tot}) *vs.* impact energy (ΔE_b^*), (c) specific energy dose (D_{ig}) and activation energy dose (D_{ig}^*) *vs.* impact energy (ΔE_b^*).

a potential function of the form $t_{ig} = A\,\nu_R^{\,B}$ the best fit in Fig. 6a exhibited a dependency on the power of −4.6 ± 1.0. The lower exponential factor indicates that a greater amount of energy in total is required to initiate a reaction when the kinetic energy of a single collision is lower. Besides, at 200 rpm the deviations in t_{ig} between identical experiments is much greater than at higher rotation speeds. Both observations could be attributed to either an increase in the elastic portion of a collision, the adoption of less efficient motion patterns by the balls[45] or a higher contribution of friction at low rotation speeds.[46]

Additionally, it is important to determine the impact energy threshold E_0, which is required to initiate an activation in the powder and ultimately trigger the combustion.[47] The E_0 can be obtained by plotting the reciprocal of N_{tot} against the ΔE_b^*.[39] A linear correlation emerges when the rotation speed is varied while maintaining all other parameters constant, as shown in Fig. 6b. The intercept of the best linear fit with the *x*-axis yields an E_0 of 2.0 ± 1 mJ.

$$\Delta E_b^* = 8m_b\left(\frac{\pi\nu_R}{60}\right)^2\left(4\left(R_J-\frac{d_b}{2}\right)^2+R_P\left(R_J-\frac{d_b}{2}\right)\right)\varphi_b \qquad (1)$$

$$N_{tot} = f_b \times N_b \times t_{ig} = \frac{K\nu_R N_b t_{ig}}{20} \qquad (2)$$

The lower milling efficiency at less energetic impacts is underlined by considering the specific energy dose (D_{ig}), calculated according to eqn (3), which quantifies the mechanical energy transferred to the powder until the MSR initiates.[39] As depicted in Fig. 6c, D_{ig} decreases with increasing impact energy and converges around 4.5 kJ g^{-1}. When the minimum energy required to initiate the ignition E_0 is subtracted from the ΔE_b^* for each collision, the activation energy dose (D_{ig}^*) can be calculated according to eqn (4). The values obtained and presented in Fig. 6c are nearly constant at 4.2 kJ g^{-1}, demonstrating the invariance of the milling energy dose for MSR reactions when the activation threshold E_0 is taken into account. As soon as the threshold of D_{ig}^* is reached, the ignition inside the milling jar can be expected, which allows the calculation of the required milling time under different conditions.

$$D_{ig} = \frac{N_b f_b t_{ig}\Delta E_b^*}{m_p} \qquad (3)$$

$$D_{ig}^* = \frac{N_b f_b t_{ig}\left(\Delta E_b^* - E_0\right)}{m_p} \qquad (4)$$

Even for other types of ball mills, the length of the activation phase or the minimum requirements on the mill can be estimated based on E_0 and D_{ig}^*. For example, in drum mills the processing can be assumed to be many free fall experiments with a gravitational acceleration and a free fall height of 55% of the drum diameter.[48] With these assumptions, the drum diameter necessary to achieve the same velocity as in the planetary mill can be calculated according to eqn (S12). The ball velocity corresponding to the minimum impact energy E_0 is 2 m s^{-1} for the 6.35 mm steel balls, which would translate in a minimum drum diameter of only 0.3 m. However, a comparison with a rotation speed of 200 rpm may be more appropriate, as the reaction was actually initiated. At this rotation speed, the ball velocity at impact is 2.4 m s^{-1} translating to a drum diameter of 0.5 m.

Furthermore, the influence of the SBR on the t_{ig} and D_{ig} was investigated for three different ball sizes (S, M, L) ranging from 3 mm to 12.7 mm in diameter. The SBR is directly related to the milling intensity, as the kinetic energy of the balls has to be distributed to a certain amount of powder. The SBR can be changed either by changing the number of balls, their density or the amount of powder.[45] In this study, the latter approach was chosen due to its high flexibility, while keeping all other parameters constant. As the ignition time can be highly sensitive to the exact experimental condition,[35] each condition was repeated at least three times (Tables S4–S6) to calculate the mean and standard deviation of the measured ignition times. While t_{ig} shows only a small deviation between identical experiments for balls with 6.35 and 12.7 mm in diameter, its deviation is larger for the 3 mm balls (Fig. 7a).

Open Access Article. Published on 15 December 2025. Downloaded on 1/7/2026 11:21:34 AM.
This article is licensed under a Creative Commons Attribution 3.0 Unported Licence.

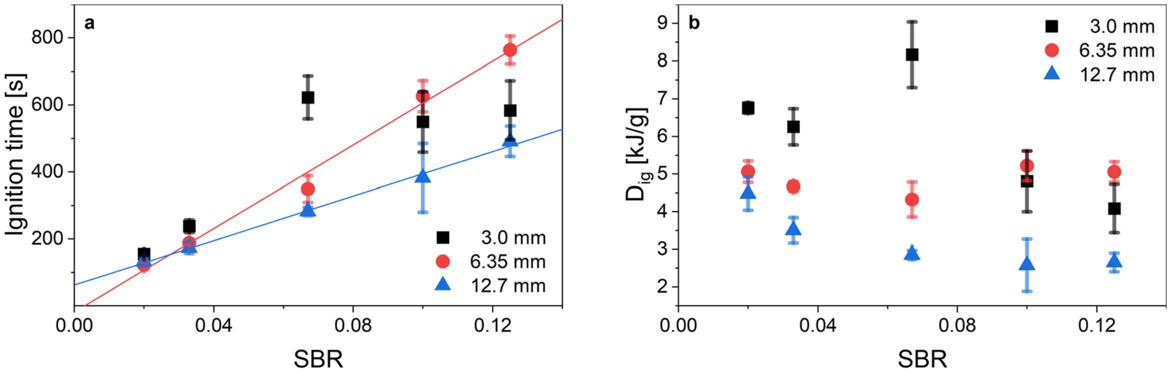

Fig. 7 Impact of the SBR and ball size on (a) the ignition time and (b) the specific energy dose of the mechanochemical reaction between LCO and Al using 65 g of balls, LCO/Al = 1.0 and a rotation speed of 650 with repeating cycles of 5 minutes milling and 5 min resting.

A linear increase is observed for the large and medium-sized balls, which is expected since the power input is assumed to remain constant for identical milling parameters (rotation speed, ball size, and number of balls). However, as the powder mass increases, the parameter t_{ig} also rises, since the power must be distributed across the growing powder mass. In contrast, when small balls are used, a linear increase is only visible at a SBR below 0.07, while at a higher SBR, t_{ig} does not increase anymore. This shift in the trend may indicate a change in ball movement or how energy is transferred to the powder. For instance, the ratio of friction to collision forces could change.

Based on the values of t_{ig}, D_{ig} can be calculated according to eqn (3) to evaluate the milling efficiency. Assuming the powder requires always the same degree of activation before the ignition, a constant value would be expected for D_{ig}. As it is shown in Fig. 7b this is true for the medium-sized balls, where the average specific energy dose is 4.8 kJ g^{-1}.

In case of the large balls, D_{ig} first decreases until it converges around 2.7 kJ g^{-1}. At a low SBR, only a small fraction of the high impact energy can be absorbed by the powder, resulting in an activation, while a significant fraction dissipates as heat. With an increasing SBR, more powder will be trapped within a single collision, and more of the impact energy can be absorbed by he powder. This, in turn, leads to a reduction in the generation of heat, thereby enhancing the milling efficiency.

For the small balls, D_{ig} shows a maximum in Fig. 7b at a SBR of 0.067, marking this milling condition as outstanding inefficient. However, despite this maximum, a generally decreasing trend with increasing SBR is observed and at high SBR, the small balls show a lower D_{ig} than the medium-sized balls. The impact energy of a single collision between a small ball and the wall (2.9 mJ) is only slightly higher than E_0 (2.0 mJ). Similar to the low rotation speed for the medium-sized balls, the activation may not be efficient. With an increasing SBR, the already low impact energy is distributed over an increasing amount of powder, and t_{ig} increases disproportionately leading to a decreasing efficiency. However, this does not provide a satisfactory explanation for the observed plateau in Fig. 7a. It is possible that the high surface area of the small balls could have a significant influence. The majority of the powder might be attached to the balls and due to the low impact energy, the exchange between attached and unattached powder might be low. This could result in an inhomogeneous activation and ultimately in unpredictable t_{ig}. Moreover, the large amount of small balls result in significant high contribution of frictional forces.[49] Since the used model exclude these contribution, the calculated energies might not be accurate.

Influence of graphite

After the investigation of the milling parameters and the kinematic analysis of the pure reaction, it is important to examine the influence of additives. In the industrially produced black mass, graphite from anode is the second largest fraction by mass.[50] To test its influence on the process, the weight fraction of graphite in the starting powder was increased from 0–60 wt% while keeping all other parameters constant. In these experiments, 2.0 g of powder mixture was milled with 6.35 mm balls at a SBR of 0.033. The medium-sized balls were used due to the fact that the SBR does not have a high impact on the efficiency. The rotation speed was set to 950 rpm, which is the maximum recommended speed for this ball size, to achieve the fastest reactions.

The spike in pressure can be detected for the graphite-free experiment after a t_{ig} of 50 s, which increased to 167 s for 10 wt% graphite content. However, when the graphite content is increased further, no spike in pressure can be detected within 1 h and only the zig-zag profile in temperature and pressure produced by the alternating milling and resting cycles are measured (Fig. S4). The XRD analysis after 10 min (Fig. 8a) reveals complete consumption of LCO in the first two patterns (0 wt% and 10 wt% of graphite) and the formation of metallic cobalt, matching the patterns of the MSR process in Fig. 4 after 60 min of milling. At a graphite content of 20 wt%, the reflections of metallic cobalt indicate the reduction of LCO, but additionally, a high fraction of intermediate Li-containing cubic cobalt oxide phase[33] and pristine LCO is also visible.

With further increasing graphite content, the reflections corresponding to metallic cobalt and cobalt oxide become less pronounced and LCO remains visible as the main phase. Pristine graphite shows an intense reflection around 12 degrees of 2 Theta caused by the stacking of honeycomb-like carbon layers[51] (Fig. S5).

© 2025 The Author(s). Published by the Royal Society of Chemistry

Open Access Article. Published on 15 December 2025. Downloaded on 1/7/2026 11:21:34 AM.
This article is licensed under a Creative Commons Attribution 3.0 Unported Licence.

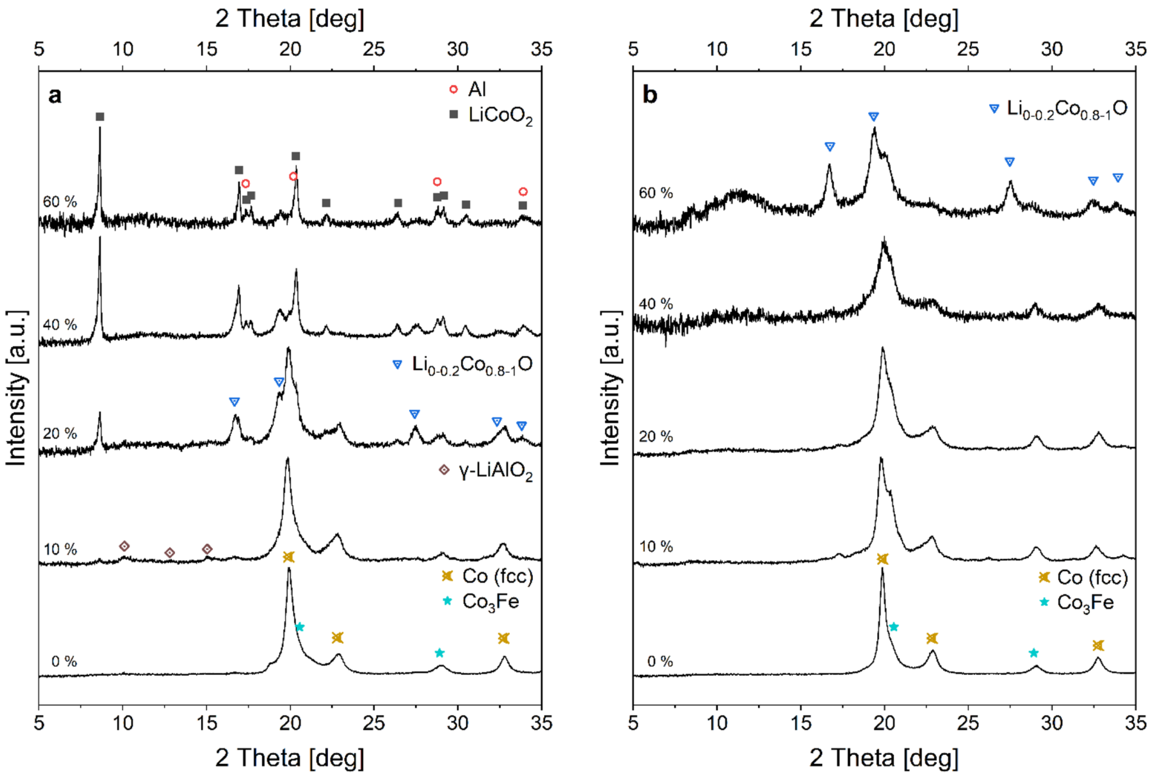

Fig. 8 XRD patterns of the mechanochemical reduction of LCO with Al alongside 0–60 wt% of graphite after (a) 10 min and (b) 60 min of milling. 2.0 g of powder was milled with 60 balls of 6.35 mm diameter, a SBR of 0.033, LCO/Al = 1.0 at 950 rpm in repeating cycles of 5 minutes milling and 5 min resting.

However, after 10 min of milling, this reflection is hardly visible in any XRD patterns of Fig. 8 indicating the graphite's exfoliation to a disordered structure. The γ-LiAlO$_2$ phase is only slightly visible in the XRD with 10 wt% graphite, while it is not yet formed or already amorphized in the other patterns.

After 60 min of milling, the absence of the 003 reflection at 8.6 degree of 2 Theta, indicates full consumption of LCO in all five experiments (Fig. 8b). However, between 0 wt% and 40 wt% graphite content, the patterns appear roughly identical, showing reflections corresponding to metallic cobalt and a second phase which could be a Co–Fe alloy. In contrast at 60 wt% graphite, the reflections of a Li-containing cobalt oxide phase dominate the pattern.

Between a graphite content of 10 and 20 wt%, the disappearance of the pressure spike indicates suppression of the combustive, self-propagating behavior in the MSR reaction (Fig. S4). This observation is consistent with the XRD results, which confirm that, at 20 wt% graphite content and above, the LCO is not consumed in a single rapid reaction. Instead, the cathode material is slowly reduced by the aluminum, first forming a Li-deficient intermediate and then subsequently transforming into metallic cobalt. Graphite does not appear to participate directly in the reaction and can be seen as an inert additive, even though it modifies the reactions mechanism.

In the suppression of the MSR, some factors must be considered. Graphite can cover the surface of the reactants and consequently reduce their contact area, thereby slowing down the reaction rate.[52] Inert additives can reduce the tendency to form agglomerates,[53] which are crucial to generate the initial heat for the ignition and can act as an insulator by reducing the contact between activated reactants. Chakurov[53] introduced the concept of a critical agglomerate radius, below which no self-propagating behavior is possible. Graphite could slow down the growth of the agglomerates, thus increasing the activation time and diluting the reaction, which in turn results in a lower heat release per gram of powder.

Even in the presence of graphite, the mixture still becomes activated during milling and can reach the threshold for a reaction. However, the reaction heat released from the powder trapped in a collision is not sufficient to ignite the surrounding powder, and the reaction remains localized to a small area. Consequently, the result is a local heating rather than a rapid increase in the overall temperature, which is insufficient to melt the cobalt.

Another important characteristic of graphite is layered structure in combination with the tendency to exfoliate, which makes it well suited as a solid lubricant.[54] Lubricants can alter the balls trajectory[43] and reduce friction. As a result, less energy is transferred to the system and local hotspots are reduced.[55] The reduced contact area between reactants, less agglomeration and less friction delay the ignition time and could eventually suppress the ignition.

The suppression of the MSR process by graphite may be of great importance for scaling up of the process to an industrial

Open Access Article. Published on 15 December 2025. Downloaded on 1/7/2026 11:21:34 AM.
This article is licensed under a Creative Commons Attribution 3.0 Unported Licence.

level. In the absence of the self-propagating reaction, the heat release is distributed over a longer timescale, thereby diminishing the increase in internal temperature. Consequently, no significant pressure builds up, and the reaction becomes safer and more controllable.

Conclusion

The mechanochemical reaction of $LiCoO_2$ with Al to produce metallic cobalt and $LiAlO_2$ using a planetary ball mill was investigated systematically, with *in situ* measurements of the internal temperature and pressure. The reaction was found to proceed *via* a mechanically induced self-propagating reaction (MSR) pathway, during which the starting materials underwent the following sequence of transition. After the activation phase, a collision initiates a reaction in a localized area. The released heat ignites the surrounding activated powder, and a combustion front spread through the volume. The majority of starting powder transforms into metallic cobalt and $LiAlO_2$ in a very short time, but not all LCO converts at this stage of reaction, and a part of it exists as a Li-containing Co(II) oxide phase. Further milling then leads to a complete conversion but crushes the large metallic pieces and degrades the crystalline structure of $LiAlO_2$. This mechanism results in a rapid increase in internal temperature and pressure.

The characteristic ignition time, detected by a spike in pressure, was used to precisely determine the length of the activation stage and allows a kinematic analysis. The minimum impact energy E_0 was calculated to be as low as 2.0 mJ per hit, indicating that even small drum mills could provide enough energy to induce the reaction. The kinematic analysis further shows the process becomes more efficient with increasing impact energy, which can be achieved by higher rotation speeds or larger ball diameters.

The effect of graphite was found to be crucial for improving the control over reaction conditions. Small amounts of graphite prolong the activation stage, but at a mass fraction of 20 wt% or higher, the self-propagating behavior is suppressed, and a more linear profile is observed. At the same time, the temperature increase is diminished, preventing a fast pressure build up. Therefore, the process can be suitable not only to pure materials but also shows a high potential for processing back mass to selectively extract lithium by a subsequent aqueous leaching.

Author contributions

R. S. guided the study, performed experiments, collected and visualized data and contributed to its interpretation, wrote the initial draft of the manuscript and conducted revisions; A. B. contributed to data interpretation and revision of the manuscript; O. D. conceived the idea and methodology and contributed to revision of the manuscript; T. B. performed ICP-OES measurements; U. G. performed SEM and EDX measurements; M. K. supervised the study, contributed to data interpretation and revision of the manuscript; H. E. contributed to revision of the manuscript. All authors provided comments during preparation of the manuscript.

Conflicts of interest

There are no conflicts to declare.

Data availability

The data supporting this article have been included as part of the supplementary information (SI). Supplementary information: detailed description of the kinematic calculations and the exact grinding parameters of the individual experiments with the calculated results. Furthermore, temperature and pressure profiles, additional microscopy images, and EDX spectra of the samples from the reaction of LCO with Al are shown. In addition, results from ICP-OES analyses and a comparative diffractogram of graphite are presented. See DOI: https://doi.org/10.1039/d5mr00092k.

Acknowledgements

This work was facilitated through funding by the RHINOCEROS project. RHINOCEROS is funded by the European Union under Grant Agreement No. 101069685. Views and opinions expressed are however those of the author(s) only and do not necessarily reflect those of the European Union or the European Climate, Infrastructure and Environment Executive Agency (CINEA). Neither the European Union nor the granting authority can be held responsible for them. This work contributes to the research performed at CELEST (Center for Electrochemical Energy Storage Ulm-Karlsruhe). Open Access funding enabled and organized by Project DEAL.

References

1 T. Tawonezvi, M. Nomnqa, L. Petrik and B. J. Bladergroen, *Energies*, 2023, **16**, 1365.
2 H. Bae and Y. Kim, *Mater. Adv.*, 2021, **2**, 3234–3250.
3 P. Kalungi, Z. Yao and H. Huang, *Materials*, 2024, **17**, 4389.
4 H. Ji, J. Wang, J. Ma, H.-M. Cheng and G. Zhou, *Chem. Soc. Rev.*, 2023, **52**, 8194–8244.
5 European Parliament and European Council, *Off. J. Eur. Communities: Legis.*, 2023, **191**, 1–117.
6 M. Bruno and S. Fiore, *Batteries*, 2023, **9**, 231.
7 M. Compagnoni, M. Grazzi, F. Pieri and C. Tomasi, *Environ. Resour. Econ.*, 2025, **88**, 43–76.
8 V. Rizos and P. Urban, *Resour., Conserv. Recycl.*, 2024, **209**, 107800.
9 S. Kim, J. Bang, J. Yoo, Y. Shin, J. Bae, J. Jeong, *et al.*, *J. Cleaner Prod.*, 2021, **294**, 126329.
10 L. Li, Y. Li and G. Zhang, *Separations*, 2024, **11**, 196.
11 L. Brückner, J. Frank and T. Elwert, *Metals*, 2020, **10**, 1107.
12 V. Marcinov, J. Klimko, Z. Takáčová, J. Piroškova, A. Miškufová, M. Sommerfeld, *et al.*, *Metals*, 2023, **13**, 1213.
13 D. Geiß, O. Dolotko, S. Indris, C. Neemann, A. Bologa, T. Bergfeldt, *et al.*, *RSC Mechanochem.*, 2024, **1**, 349–360.
14 F. Rao, Z. Sun, W. Lv, X. Zhang, J. Guan and X. Zheng, *Waste Manage.*, 2023, **156**, 247–254.

© 2025 The Author(s). Published by the Royal Society of Chemistry

Open Access Article. Published on 15 December 2025. Downloaded on 1/7/2026 11:21:34 AM.
This article is licensed under a Creative Commons Attribution 3.0 Unported Licence.

15 O. Dolotko, I. Z. Hlova, Y. Mudryk, S. Gupta and V. P. Balema, *J. Alloys Compd.*, 2020, **824**, 153876.

16 O. Dolotko, N. Gehrke, M. Knapp and H. Ehrenberg, *J. Alloys Compd.*, 2024, **976**, 172884.

17 P. Baláž, *Mechanochemistry in Nanoscience and Minerals Engineering*, Springer Berlin Heidelberg, Berlin, Heidelberg, 2008.

18 O. Dolotko, N. Gehrke, T. Malliaridou, R. Sieweck, L. Herrmann, B. Hunzinger, *et al.*, *Commun. Chem.*, 2023, **6**, 49.

19 T. Wu, G. Lahiner, C. Tenailleau, B. Reig, T. Hungria, A. Esteve, *et al.*, *Chem. Eng. J.*, 2021, **418**, 129432.

20 G. B. Schaffer and P. G. McCormick, *Metall. Trans. A*, 1990, **21**, 2789–2794.

21 A. Bakhshai, R. Pragani and L. Takacs, *Metall. Mater. Trans. A*, 2002, **33**, 3521.

22 T. F. Grigoreva, T. Yu. Kiseleva, S. A. Petrova, T. L. Talako, S. V. Vosmerikov, T. A. Udalova, *et al.*, *Phys. Met. Metallogr.*, 2021, **122**, 572–578.

23 J. E. Oghenevweta, D. Wexler and A. Calka, *Mater. Charact.*, 2018, **140**, 299–311.

24 L. Takacs, *Faraday Discuss.*, 2014, **170**, 251–265.

25 F. J. Gotor, M. Achimovicova, C. Real and P. Balaz, *Powder Technol.*, 2013, **233**, 1–7.

26 M. Baláž, R. Džunda, R. Bureš, T. Sopčák and T. Csanádi, *RSC Mechanochem.*, 2024, **1**, 94–105.

27 J. Vauloup, C. Bouilhac, N. Coppey, P. Lacroix-Desmazes, B. Fraisse, L. Stievano, *et al.*, *RSC Mechanochem.*, 2024, **1**, 393–401.

28 F. de la Peña, E. Prestat, V. T. Fauske, J. Lähnemann, P. Burdet, P. Jokubauskas and *et al.*, *Hyperspy/Hyperspy: v2.1.1 Version v2.1.1*, 2024, DOI: 10.5281/zenodo.12724131.

29 E. A. Owen and D. M. Jones, *Proc. Phys. Soc. B*, 1954, **67**, 456–466.

30 Z. Xie, S. Ni and M. Song, *Powder Technol.*, 2018, **324**, 1–4.

31 M. Okayasu and S. Tomida, *Materials Sci. Eng. A*, 2017, **684**, 712–725.

32 N. H. Amirkhanyan, M. K. Zakaryan, S. L. Kharatyan, A. Yeghishyan, M. Zhukovskyi, A. Aprahamian, *et al.*, *Mater. Chem. Phys.*, 2024, **319**, 129368.

33 W. D. Johnston, R. R. Heikes and D. Sestrich, *J. Phys. Chem. Solids*, 1958, **7**, 1–13.

34 L. Takacs, *Prog. Mater. Sci.*, 2002, **47**, 355–414.

35 M. Carta and F. Delogu, *Phys. Chem. Chem. Phys.*, 2024, **26**, 12316–12323.

36 M. S. Ortman and E. M. Larsen, *J. Am. Ceram. Soc.*, 1983, **66**, 142–144.

37 A. N. Sembira and J. G. Dunn, *Thermochim. Acta*, 1996, **274**, 113–124.

38 Q. Meng, K. Zhang, R. He and Z. Qu, *Int. J. Appl. Ceram. Technol.*, 2024, **21**, 3789–3811.

39 L. Caggiu, S. Enzo, L. Stievano, R. Berthelot, C. Gerbaldi, M. Falco, *et al.*, *Batteries*, 2020, **6**(3), 43.

40 N. Burgio, A. Iasonna, M. Magini, S. Martelli and F. Padella, *Il Nuovo Cimento D*, 1991, **13**, 459–476.

41 M. Kessler and R. Rinaldi, *Front. Chem.*, 2022, **9**, 816553.

42 M. Mhadhbi, *Adv. Mater. Phys. Chem.*, 2021, **11**, 31–44.

43 A. V. Aborkin, A. I. Elkin, V. V. Ryabkova, A. P. Bugayov and M. I. Alymov, *Metallurgist*, 2025, **69**, 147–157.

44 E. Gil-González, M. D. R. Rodríguez-Laguna, P. E. Sánchez-Jiménez, A. Perejón and L. A. Pérez-Maqueda, *J. Alloys Compd.*, 2021, **866**, 158925.

45 E. Chicardi, F. J. Gotor, M. D. Alcalá and J. M. Córdoba, *Powder Technol.*, 2017, **319**, 12–18.

46 C. Real and F. J. Gotor, *Heliyon*, 2019, **5**, e01227.

47 C. Deidda, F. Delogu, F. Maglia, U. Anselmi-Tamburini and G. Cocco, *Materials Sci. Eng. A*, 2004, **375–377**, 800–803.

48 H. Zoz, H. Ren, R. Reichardt and H. U. Benz, *High Energy Milling/Mechanical Alloying/Reactive Milling*, https://group.zoz.de/zoz.main/pdf_content/publications/v14.pdf, accessed October 24, 2024.

49 C. Suryanarayana, *Prog. Mater. Sci.*, 2001, **46**, 1–184.

50 A. Vanderbruggen, E. Gugala, R. Blannin, K. Bachmann, R. Serna-Guerrero and M. Rudolph, *Miner. Eng.*, 2021, **169**, 106924.

51 P. G. Schiavi, L. D'Annibale, A. G. Marrani, F. Amato, O. Russina, S. Iacobelli, *et al.*, *Carbon*, 2025, **238**, 120295.

52 S. G. Zhu, C. X. Wu and Y. L. Luo, *J. Mater. Sci.*, 2010, **45**, 1817–1822.

53 C. Chakurov, V. Rusanov and J. Koichev, *J. Solid State Chem.*, 1987, **71**, 522–529.

54 A. Pragatheeswaran, R. Ravi and S. R. Bakshi, *Adv. Powder Technol.*, 2019, **30**, 2759–2767.

55 Y. Chen, P. Renner and H. Liang, *Friction*, 2023, **11**, 489–512.

© 2025 The Author(s). Published by the Royal Society of Chemistry